ARCHIVIO ISTITUZIONALE
DELLA RICERCA

Alma Mater Studiorum Università di Bologna
Archivio istituzionale della ricerca

Accurate transmission performance evaluation of servo-mechanisms for robots

This is the final peer-reviewed author's accepted manuscript (postprint) of the following publication:

Published Version:
Bilancia, P., Monari, L., Raffaeli, R., Peruzzini, M., Pellicciari, M. (2022). Accurate transmission performance evaluation of servo-mechanisms for robots. ROBOTICS AND COMPUTER-INTEGRATED MANUFACTURING, 78, 1-11 [10.1016/j.rcim.2022.102400].

Availability:
This version is available at: https://hdl.handle.net/11585/949355 since: 2024-02-08

Published:
DOI: http://doi.org/10.1016/j.rcim.2022.102400

Terms of use:

Some rights reserved. The terms and conditions for the reuse of this version of the manuscript are specified in the publishing policy. For all terms of use and more information see the publisher's website.

This item was downloaded from IRIS Università di Bologna (https://cris.unibo.it/).
When citing, please refer to the published version.

(Article begins on next page)

21 February 2025

This is the final peer-reviewed accepted manuscript of:

Pietro Bilancia, Luca Monari, Roberto Raffaeli, Margherita Peruzzini, Marcello Pellicciari, Accurate transmission performance evaluation of servo-mechanisms for robots, Robotics and Computer-Integrated Manufacturing, Volume 78, 2022, 102400, ISSN 0736-5845.

The final published version is available online at:

https://doi.org/10.1016/j.rcim.2022.102400

Terms of use:

Some rights reserved. The terms and conditions for the reuse of this version of the manuscript are specified in the publishing policy. For all terms of use and more information see the publisher's website.

This item was downloaded from IRIS Università di Bologna (https://cris.unibo.it/)

When citing, please refer to the published version.

Accurate Transmission Performance Evaluation of Servo-Mechanisms for Robots

Pietro Bilancia[a,*], Luca Monari[b], Roberto Raffaeli[a], Margherita Peruzzini[c] and Marcello Pellicciari[a]

[a]Department of Sciences and Methods for Engineering, University of Modena and Reggio Emilia, Reggio Emilia, 42122, Italy.
[b]K-LOOPS S.R.L., Modena, 41125, Italy.
[c]Department of Engineering Enzo Ferrari, University of Modena and Reggio Emilia, Modena, 41125, Italy.

ARTICLE INFO

Keywords:
Test Rig
Experimental Methods
Servo-Mechanisms
Robot Reducers
Torque Ripples
Transmission Error
Lubricant Temperature

ABSTRACT

The Servo-Mechanisms (SMs) mounted in industrial robots joints are a major source of positioning accuracy errors. To improve robots precision performance, researchers have been focusing on the development of novel SMs design and control strategies, which need extensive experimental analyses to tune their parameters. In this context, the scope of this paper is double: first, to present the novel experimental apparatus and methods designed to improve the accuracy of the transmission performance evaluation of high dynamics SMs and, secondly, to report and discuss the achieved experimental results. In the first part, a description of the test rig tuning operations is given, primarily focusing on the signals synchronization and on the elimination of the measuring errors caused by the mechanical transmission elasticity and the servomotor torque ripples. Then, control strategies for compensating the torque ripples and input speed errors are defined. It is shown that speed oscillations can be reduced of $\approx 70\%$ when rotating the servomotor up to 2000rpm, improving the measurement quality of the reducer performance. In the second part, a set of experiments is carried out to assess the combined effect of input speed and lubricant temperature on the reducer behavior. The system sensitivity to the variation of the input parameters is confirmed by the dynamic lost motion curves, whose mean value equals $16.8''$ and $35.4''$ when the reducer is operated at its minimum and maximum friction load respectively. At last, the extrapolated harmonic content is used to build a simple mathematical model of the reducer transmission error.

1. Introduction

In the last years, to comply with the growing demand of modern markets, Industrial Robots (IRs) have become the central elements of many automated production plants owing to their high operational effectiveness, large degree of flexibility and extended workspace [1, 2]. To perform precise operations, ensure a high quality of the manufactured parts and reduce the waste of material, much attention has been recently placed on the IRs positioning performance [3–8]. This is primarily governed by the Servo-Mechanisms (SMs) embedded in the robots joints, consisting of a servomotor and a speed reducer [2, 9]. The major problems with the servomotors and related drive systems are: i) curve tracking error [10, 11], ii) unmodeled high order electromechanical effects [12] and iii) torque ripples [13]. The first can partially be addressed by implementing adaptive control laws [14], whereas the remaining ones require the definition of proper compensation strategies [15]. From the control point of view, one must also deal with the nonlinearities introduced by the gear transmission [16]. Among the existing classes available in the market (see [17] for a review), cycloidal reducers are getting much more attention from IR manufacturers due to their compact size and higher robustness. The most used option, named Rotate Vector (RV) reducer, is a two stages solution consisting of a planetary gear followed by a cycloid-pin gear [18]. Both stages cause undesired hysteretic behavior as a result of the transmission backlash and compliance [19, 20]. The so-called "double valued nonlinearity" originated from the backlash directly affects the robot accuracy and creates important control challenges [21]. The combined effect of backlash and compliance is evaluated through the Transmission Error (TE) and the Lost Motion (LM) [22, 23], i.e. the industry-accepted standard performance indexes for the reducers accuracy. It should be noted that well-behaved reducers would present minimum (ideally null) values of TE and LM.

To overcome the above discussed SMs limitations, previous studies have been focused on the redesign of the reducer internal parts (e.g. tooth shape optimization [24–26] and machining/assembly tolerances correction [27, 28]), the implementation of load-side feedback sensors [29] or the definition of model-based feedforward compensations [30, 31]. The first approach has led to a number of promising design concepts. The proposed solutions, actually tested on research lab prototypes, support the development of new reducers but cannot be applied to the existent industrial plants as each IR would need to be disassembled to enable parts substitution. The second approach is simple and intuitive but, similarly to the first one, it would raise the plant setup time and cost considerably. The latter approach is less expensive during the implementation phase even though, for definition, it necessarily requires the development of high fidelity behavioral models. Previous research works have formulated either theoretical [32–34] or simulation-based [35, 36] models capable of capturing the reducers nonlinearities. However, the inherent complexity of the reducer

pietro.bilancia@unimore.it (P. Bilancia)
ORCID(s): 0000-0002-4931-1745 (P. Bilancia)

assembly and the rather limited availability of detailed drawings (tolerances and installation aspects, normally hidden from vendors) make it difficult to develop exact correlations between geometric/functional parameters and output performance. A crucial point, usually missed in merely kinematic analyses, is the lubrication state of the transmission [26, 37]. In fact, the RV reducers case is filled with great amount of lubricant (accurately chosen and specified by manufacturers), which aids in reducing parts wear but also introduces non-negligible speed and temperature dependent viscous friction effects that impact the TE [38].

For a deep understanding of the RV reducer dynamics, experimental campaigns become essential, also in view of determining accurate empirical models which can be readily exploited for compensation purposes. The transmission performance of precision reducers has been already tested, investigating the influence of speed [39], external load [22] and state of degradation [40]. Other studies have defined practical strategies for compensating manufacturing and assembly errors of the measuring system [41–43]. The referenced works have provided valuable standards and metrics for the performance testing of precision reducers, though a series of important aspects have not been yet sufficiently discussed. First of all, these works lack of accurate descriptions regarding the adopted measuring methods and tools. There is no mention of the rig tuning process, and the speed state at the reducer input side is claimed constant because the servomotor is controlled in speed mode. However, this may not be always the case since proper actions must be taken to suppress the servomotor disturbs and avoid the shaft vibrations [44]. These phenomena strongly compromise the TE measurement and deserve consideration. Other research gaps can be noticed in terms of parameters selection and results interpretation. For example, the influence of lubricant temperature on the reducer behavior is not appropriately documented neither in previous studies nor in product catalogs. Even so, the relevant impact of such parameter on the performance of heavy duty IRs has been shown experimentally in [45].

Based on these considerations, the novel contributions of this paper are as follows:

- To provide a detailed description of the instrumentation and experimental methods employed to assess the SMs performance.
- To report practical guidelines and compensation approaches for stabilizing the reducer input speed and thus extending the measurement accuracy.
- To quantitatively assess the effect of the lubricant temperature and input speed on the reducer behavior.

The extrapolated data will support the validation of existing methods and tools aimed at optimizing the SMs performance [46], and the development of new kinematic compensation models.

The remaining of the paper is structured as follows: Section 2 describes the utilized experimental equipment,

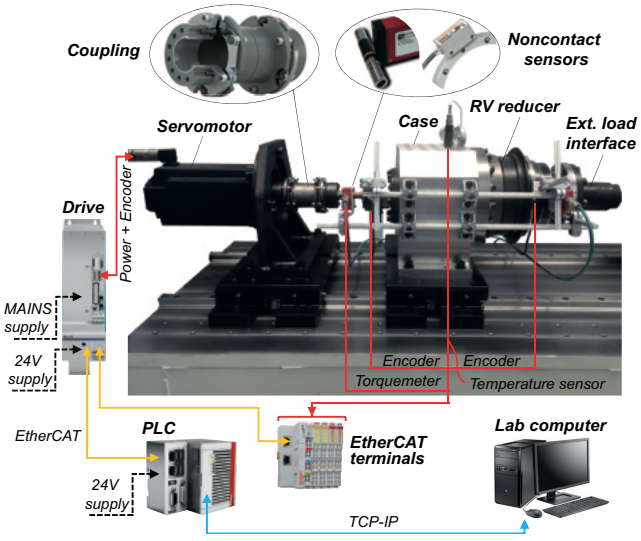

Figure 1: Schematic of the test rig: equipment overview and main connections.

Section 3 deals with the rig performance identification and tuning, whereas Section 4 reports the RV reducer experimental results. The concluding remarks are given in Section 5.

2. Experimental setup

This section provides a detailed description of the test equipment utilized for the experimental characterization of industrial SMs.

2.1. Test rig

The test rig, whose schematic is depicted in Fig. 1, has been conceived to perform several experiments so as to effectively analyze the effect of each parameter under different working conditions. Compared to the existent arrangements (summarized in [38]), the novel rig design, thoroughly discussed in [47], provides the following advantages:

- Flexibility of operation: the modular layout and the use of quick mechanical connections allow to reconfigure the measuring chain with minimum effort and promote the execution of different types of tests (with a specific subset of parts, if required).
- Compatibility with many devices: the rig can test commercial SMs of different models and sizes. To favor the installation of newly commissioned components, the customization is limited to a portion of the system (i.e. intermediate parts/flanges) thanks to a modular design approach based on the use of unified mechanical connections.
- Adaptive testing conditions: differently from the experimental setups utilizing either static or low-dynamics systems (e.g. induction motors and magnetic brakes), the proposed rig provides a mechatronic

Table 1
Relevant parameters of the installed equipment.

Equipment	Company	Model	Characteristics	Resolution/Accuracy
Servomotor	BOSCH	MS2N07-D0BHN	Rated/Max: 2000/4000rpm 22/73.2Nm	-
Servomotor encoder	ACURO link	AD58	Analogic impulses per turn: 2048	R:24bit A:25″
Drive unit	BOSCH	HMS01	Controller Pos-/Vel-/Cur-loop: 250/125/62.5μs	-
Shaft coupling	Mayr	ROBA-DS size 25	Max speed: 11800rpm Max torque: 435Nm	-
Reducer	Nabtesco	RV-160N-81	Rated/Max (output): 15/48rpm 1600/4000Nm	-
Torquemeter	Manner	Measuring flange	Max calibrated torque: 50Nm	R:16bit A: Lin. Dev. 0.08%
Optical encoder (input side)	Renishaw	Ring: RESA 100mm Readhead: RESOLUTE	Analogic impulses per turn: 10472	R:32bit A:2.86″
Optical encoder (output side)	Renishaw	Ring: RESA 200mm Readhead: RESOLUTE	Analogic impulses per turn: 20944	R:32bit A:1.43″
Thermoresistance	Industrie Technik	STIC-PT1000/135	Measuring range: -30°C...70°C	Lin. Dev. 0.41%
PLC	Beckhoff	CX5140	PLC & EtherCAT cycle time: 250μs	-

active testing load leveraging the potentialities of modern high-dynamics servomotors which accurately reproduce the realistic industrial time-varying motion and loading conditions. Modern controllers also enable the implementation of dedicated compensation strategies which aid in increasing the measurement quality, as it will be shown in Section 3.

- Additional sensors: the rig collects a great amount of inputs, including temperature data (not considered in previous works) and, if needed, vibration data with accelerometers.

The shown mechatronic system mainly consists of an electric servomotor (BOSCH MS2N07), a drive unit (BOSCH HMS01) and a robot RV reducer (Nabtesco RV 160N). The servomotor shaft is connected to the reducer input shaft by means of a multi-plate, backlash free, coupling (Mayr Roba DS). Such coupler makes use of two flexible disk packs, mounted between the left clumbing hub (motor side), the central rigid sleeve and the right clumping hub (reducer side), to correct possible slight axial, radial and angular shaft misalignments (Fig. 1). The reducer is installed on a purposely designed case that accommodates the input gear shaft and contains the required amount of lubricant for the gears.

The servomotor state is constantly monitored by the drive unit. In particular, its angular position is acquired with the integrated 24 bit encoder (ACURO link AD58), whereas the torque is estimated from the absorbed armature current. To achieve higher accuracy, an additional noncontact strain gauge torquemeter (Manner measuring shaft) is installed between the Mayr coupling and the input gear shaft, as shown in Fig. 1. A second torquemeter is fixed at the reducer output flange, though this will not be considered in this research as no external loads are applied. Then, with the aim to shorten the measurement chain and lower the sources of errors, the rig has been equipped with two 32 bit optical encoder (Renishaw RESOLUTE), respectively placed at the reducer input and output side. As it will be shown in Section 3, the transmission system is subject to slight torsional

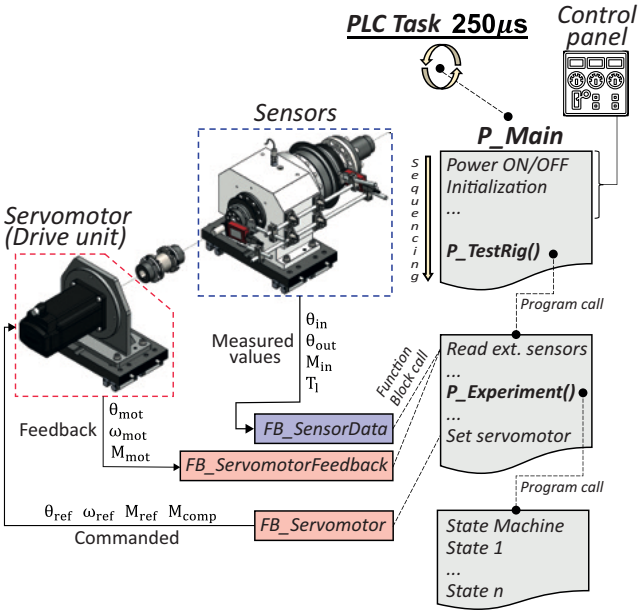

Figure 2: PLC-based acquisition software. The abbreviation *P* and *FB* are used to indicate respectively programs and function blocks.

deformations during the test, that is why the position registered with the servomotor integrated encoder cannot be considered as the reducer input position and an additional encoder is needed for the correct evaluation of the reducer transmission performance. At last, to assess the lubricant temperature, a Pt1000 thermoresistance is positioned inside the reducer case filler pipe. The main parameters of the employed instruments are specified in Table 1.

2.2. Software layout

During the experiments, the signal acquisition is handled with a Beckhoff CX5140 Programmable Logic Controller (PLC), which also operates as a position/velocity/torque setpoint generator for the closed loop servomotor controller running in the drive unit. The adopted Beckhoff technology supports all common industry standards and enables very

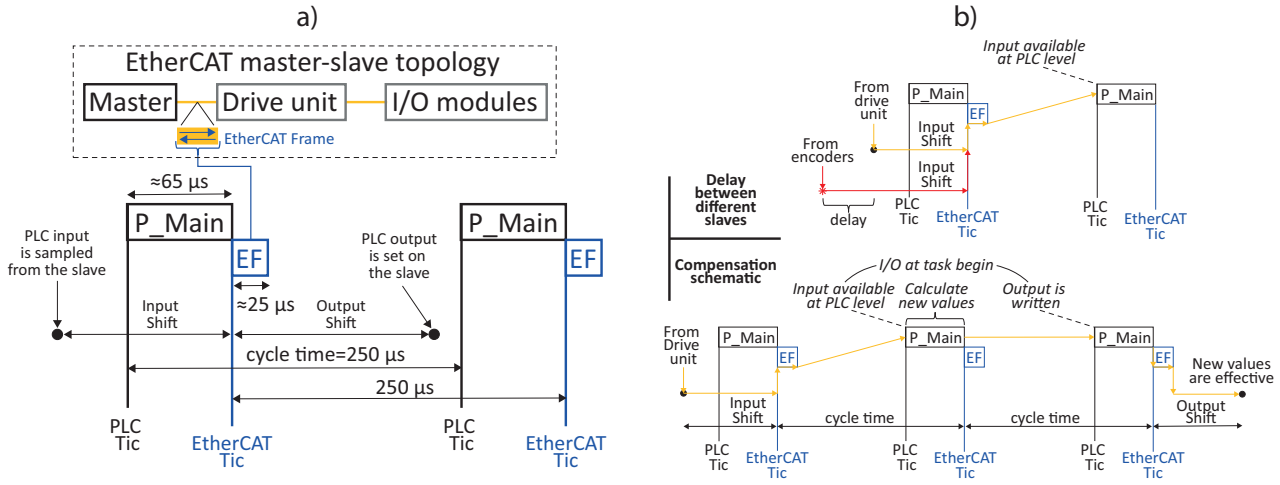

Figure 3: Time diagram of the EtherCAT network: a) Topology and principle of operation of the distributed clock; b) Practical applications.

fast and highly deterministic responses which are demanded in advanced mechatronic systems. In this way, the same measuring tools and methods can be utilized in a wide range of industrial applications.

The entire process is overseen from an industrial PC with TwinCAT, i.e. the automation software package developed by Beckhoff. With reference to Fig. 2 and following the PLC standards, the acquisition software has been divided into a set of programs and function blocks. The former mainly contain top level experimental procedures (or subordinate programs) to be executed in a precise order within the PLC task cycle, whereas the latter manage specific modules of the rig and incorporate routines for processing their information, namely sensor feedback acquisition, servomotor state/error monitoring, motion profile generation, compensation action evaluation, etc. As shown in Fig. 2, these function blocks are directly linked to the PLC Input/Output (I/O) modules and receive a new set of input values at each PLC task cycle. A real-time communication based on the EtherCAT protocol (fieldbus) is established between the PLC and the external devices (drive unit and sensors). The signals are uniformly sampled with a rate of 4000Hz (i.e. a PLC and EtherCAT task cycle time $t_{cycle} = 250\mu$s) as a consequence of the drive unit cycle time limitations. The received data set contains the angular positions read from the encoders (servomotor position θ_{mot}, reducer input position θ_{in} and reducer output position θ_{out}), the servomotor speed ω_{mot}, the torques from servomotor (M_{mot}) and torquemeter (M_{in}), and the lubricant temperature (T_l). It is noteworthy that the processing of analog inputs M_{in} and T_l require special attention. In particular, fine manual adjustments have been made on the torquemeter evaluation unit to reach the correct signal amplification. As for the Pt1000 sensor, its nonlinear characteristic curve (taken from the catalog) has been imported into the PLC environment and then used to convert the electrical resistance into accurate temperature values. Regarding the PLC outputs, based on the selected operation mode (i.e. position, velocity or torque control) and on the programmed motion profile, a dedicated function block generates new command values (θ_{ref}, ω_{ref} or M_{ref}), which are then transmitted to the drive unit via EtherCAT. In case of position or velocity control mode, following the feedforward compensation approach, one could also provide an additional torque value (M_{comp}) that takes effect in the drive unit to correct the output of the velocity loop (i.e. right before entering into the current loop). More details about this will be given in Section 3. Apart from the above mentioned real-time exchanged information, a wide range functional parameters (e.g. servomotor state and settings, winding temperature, control loop gains) can be assessed and configured via the PLC.

In the developed modular PLC framework, the experimental procedures are specified into dedicated programs (*P_Experiment* in Fig. 2). This approach offers the possibility to perform several types of experiments and to further extend the rig flexibility. In particular, each experiment can be finely customized and programmed using the standard PLC languages. To implement event-driven task execution within the PLC cyclic logical architecture, all the experiments have been programmed with a state machine approach. In this way, the transition from one experiment phase to the next is accomplished after proper verification of unique conditions (e.g. specific Boolean variables or thresholds).

2.3. Signals synchronization

The signals time synchronization is a key aspect to perform accurate measurements in a multi-sensors distributed system [41]. This problem can be examined from the PLC point of view by identifying how old is the received input value with respect to the current PLC time (input shift, t_{is}) and when the new generated output value will become effective at the slave level (output shift, t_{os}). The precise time mapping of each slave of the EtherCAT network is managed from the distributed clock function. A graphical representation of this principle is reported in Fig. 3a, where *P_Main* represents the code run at each PLC task cycle and

EF is the EtherCAT frame with I/O data passing through all the slaves. The time values specified in the schematic are accessible for the user in the TwinCAT environment. Figure 3b illustrates two practical implications of the distributed clock that deserve special attention when utilizing the shown EtherCAT topology:

1. The top schematic analyzes the periodical time delay between the position signal sampled from two different slaves, namely the servomotor integrated encoder (θ_{mot}) and the first external optical encoder (θ_{in}). A comparison of their input shift gives: $275 - 194 = 81\mu$s. This may seem negligible at first sight as both the position feedback values become available at the next PLC task cycle. However, let once suppose to run the servomotor at 1000rpm: the calculated delay, if not considered during the post-processing, would lead to an error of 0.49° between the two encoder signals, which complicates the results interpretation. It is worth mentioning that the two external encoders are acquired with a 2-Channels Beckhoff terminal and present the same input shift, which ensures precise data synchronization.
2. The bottom schematic displays the complete sequence of events of the data exchange operations between the PLC and the drive unit. Such diagram becomes extremely important, for instance, to compensate position-dependent disturbances in a highly dynamic manner. In fact, model-based online compensation strategies usually exploit lookup tables and estimate the correction to be applied at the next cycle based on the available feedback value. In this context, the exact knowledge of the signal input and output shift times allows to correctly synchronize the generated correction with the shaft angular position.

The above discussed points will be further recalled in Section 3.1 and 3.3 with practical examples.

3. Rig performance identification and tuning

3.1. Input transmission elasticity

IRs present compact and highly integrated SMs where the reducer is directly keyed on the servomotor shaft. On the other hand, the mechanical transmission typically seen in testing platforms comprises additional elements, namely a strain gauge torquemeter and a multi-plate coupling. Compared to the servomotor shaft and the reducer input shaft, such elements have relatively low torsional stiffness. Figure 4 shows a simplified lumped parameters model of the system consisting of two inertias connected through a single spring. Based on the stiffnesses specified in the components datasheets ($k_c = 110303$Nm/rad and $k_t = 13071$Nm/rad respectively for the coupling and the torquemeter), the equivalent spring constant, k_{in}, can be estimated as follows:

$$k_{in} = \left(1/k_c + 1/k_t\right)^{-1} = 11686 Nm/rad \qquad (1)$$

As for the equivalent inertial disks, the mass contributions at the reducer left side are directly summed whereas the ones

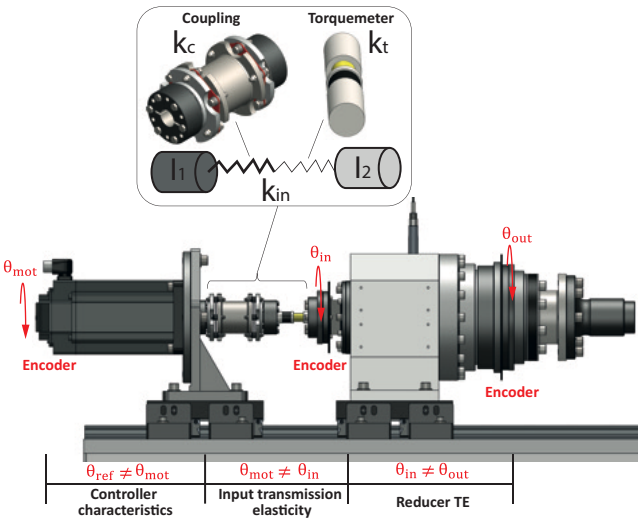

Figure 4: Angular position errors within the test rig transmission.

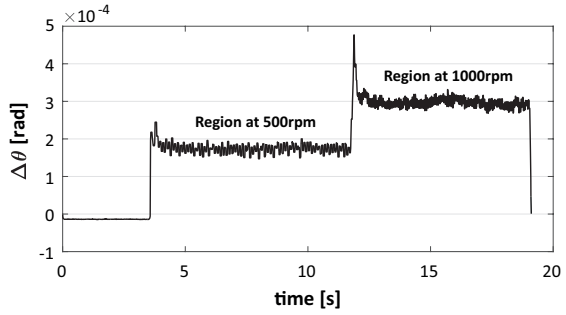

Figure 5: Resulting elastic torsional deflection of the input transmission at steady state operation.

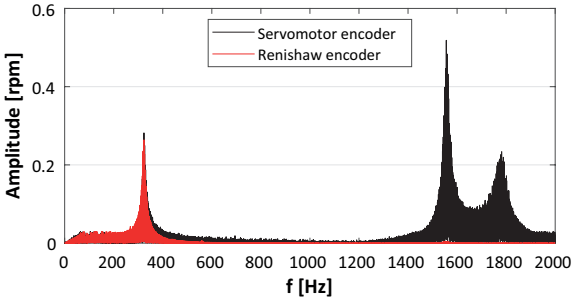

Figure 6: Spectrum of speed oscillations in case of 1Nm random excitation torque.

at the right side are firstly divided by τ^2, being $\tau = 81$ the reduction ratio of the RV reducer. By utilizing the values reported in the manufacturers catalogs, the obtained I_1 and I_2 are, respectively, $4.15e^{-3} kgm^2$ and $3.92e^{-3} kgm^2$. The introduced k_{in} influences the rig operability mainly in two ways. At first, it makes it necessary to install an additional encoder at the reducer input side since θ_{mot} cannot be taken

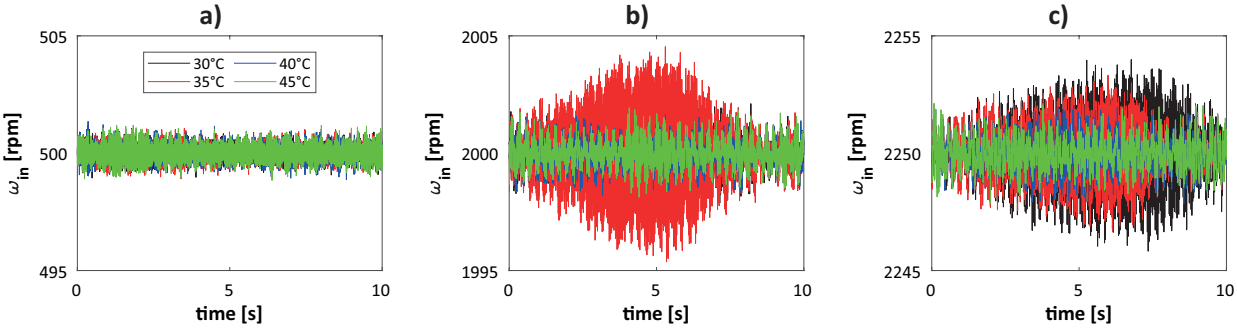

Figure 7: Effect of lubricant temperature on ω_{in}: test at a) 500rpm; b) 2000rpm and c) 2250rpm.

Table 2
RV reducer lubricant properties.

Property	Value
Density at $15°C$	$860 kg/m^3$
Viscosity at $40°C$	$155 cSt$
Viscosity Index	138

as the reducer input position. This is clearly shown in Fig. 5, where the servomotor is run at 500 and 1000rpm and the resulting angular deflection at steady state (calculated as $\Delta\theta = \theta_{in}(t + 81\mu s) - \theta_{mot}(t)$, see Fig. 3b) is $1.7e^{-4}$rad and $2.9e^{-4}$rad. The registered torques are 1.9Nm and 3.2Nm, which give $k_{in,exp} \approx$ 11100Nm/rad. The low value of k_{in}, together with the high acceleration set in the servomotor controller, generates peaks when a new speed is imposed via step command, as it can be noted from the plot.

More importantly, the obtained k_{in} shifts the system natural frequency down to a frequency range where possible torsional excitations may occur. The effect is an oscillatory twisting of the shaft that is superimposed to the running speed. The resulting speed fluctuations reduce the measurements quality and, if persistent, can seriously damage the rig electromechanical components. By exploiting the simplified model, the first natural frequency can be estimated as:

$$f_n = \frac{1}{2\pi}\sqrt{k_{in,exp}\frac{I_1 + I_2}{I_1 I_2}} = 373.5 Hz \qquad (2)$$

To verify this result experimentally, a test has been conducted by means of the BOSCH drive integrated command value generator. Using a pre-defined amplitude of 1Nm, an alternating torque command at random frequencies is sent to the servomotor, which excites the mechanical transmission in the range $0 - 4000$Hz. The system response in terms of angular speed has been recorded through the oscilloscope tool and then processed with a Fast Fourier Transform (FFT). The results are shown in Fig. 6. The first peak is in the range $[330, 360]$Hz, though other important contributes (not predicted by the simplified model and only present in the feedback signal of the servomotor encoder) can be observed at $f > 1600$Hz. Given that resonances result from the excitation of natural frequencies, special attention must be paid on the possible sources of disturbance arising from the drive unit and the servomotor, namely the control loops actions and the torque ripples. To minimize the impact of the controller, an exhaustive experimental tuning of the velocity loop proportional gain is required. Also, a careful definition of the velocity loop filters would certainly aid in the suppression of resonances. In this work, two second order band-stop filters (set within the servomotor drive software respectively at center frequencies $f_c = 350$Hz and $f_c = 1650$Hz, with bandwidth equal to $f_{BB} = 100$Hz and $f_{BB} = 300$Hz) have been chosen over the classic first order low pass filters so as not to reduce the control responsiveness and also improve the quality of the measurements. Unfortunately, the control loop without any filter is found to be unusable. The positive effect of torque ripples compensation will be discussed in Sec. 3.3.

3.2. Effect of lubricant temperature

To evaluate the influence of the RV reducer lubricant temperature on the transmission dynamic response (i.e. to include the contribution of viscous frictions), the reducer case has been filled with synthetic oil. In particular, following the manufacturer's strict indications, the Castrol Optigear Synthetic RO 150 oil has been adopted in all the experiments so as to i) characterize the reducer behavior in its certified commercial conditions and ii) avoid the deterioration of its performance (e.g. abnormal noise and irregular torque) and possible premature damages. To ensure the correct reducer functioning, the oil (whose properties are reported in Table 2) must operate in the range $[-10, 50]°C$ and present a viscosity index (defined as the rate of change of an oil's viscosity with temperature) between 135 and 140.

The servomotor is operated in speed mode between 100rpm and 2500rpm. Before starting each test, a warm-up phase is performed until the lubricant temperature is stabilized. The considered temperatures are 30°C, 35°C, 40°C and 45°C. A comparison of the speed feedback signals acquired at different lubricant temperatures is provided in Fig. 7. Only the most representative cases have been selected for the discussion. In particular, the following considerations can be drawn:

1. For $\omega_{mot} \leq$ 1500rpm, there are no critical speed oscillations in the feedback signals (Fig. 7a). This

confirms the efficacy of the imposed filters and the stability of the controller. The effects of lubricant temperature can be observed in the torque feedback signal as the resistant friction torque changes with the lubricant viscosity (see Section 4 and also [45]).

2. For $2000rpm \leq \omega_{mot} \leq 2250rpm$, an audible mechanical resonance occurs at $T_l = 30°C$ and $T_l = 35°C$ (Figs. 7b and c). As visible from the plots, increasing the lubricant temperatures will dampen the speed oscillations.
3. Within this speed range, the servomotor torque ripples are most-likely the main source of excitation. These periodic (i.e. position-dependent) torque fluctuations, resulting from geometrical, mechanical, magnetic, or current imperfections of the system, are not desired in demanding motion control since they induce speed oscillations, which can be even amplified when the pulsation frequency coincides with the natural frequency of the mechanical system (i.e. the previously calculated f_n).

To reduce the impact of torque ripples on the measurements and thus extend the rig usability, the remaining of this Section is dedicated to defining a practical approach for disturbs compensation.

3.3. Torque ripple compensation

The suppression of servomotor related disturbs has been extensively investigated from the research community. The proposed approaches can be primarily split into two main categories, namely design-oriented and control-oriented methods [48, 49]. The second category has attracted much more attention since the developed methods are applicable to the existent hardware without parts substitution and extra costs. According to [13], in this work a model-based feedforward compensation has been established to stabilize the reducer input shaft. In practice, an additive (compensating) torque command signal, M_{comp}, is generated from the PLC based on a pre-defined lookup table containing the experimental model of the servomotor disturbs as a function of θ_{mot}. Following the bottom schematic of Fig. 3b, at the i-th PLC task cycle the torque value M^i_{comp} is obtained as:

$$M^i_{comp} = \begin{cases} k_c M^f_{model}(\theta_{est}), & \omega_{mot} > 0 \\ k_c M^b_{model}(\theta_{est}), & \omega_{mot} < 0 \end{cases} \tag{3}$$

where M_{model} is the experimental model (^{f} and ^{b} indicate forward and backward rotation) stored in the lookup table, k_c is a user-defined proportional gain (by default equal to 1) and θ_{est} is the estimated future rotor angular position, calculated as:

$$\theta_{est} = \theta_{mot} + (t_{is} + t_{os} + 2t_{cycle})\omega_{mot} \tag{4}$$

where θ_{mot} is the encoder value currently available at PLC level, whereas $t_{is} = 194\mu$s, $t_{os} = 306\mu$s and $t_{cycle} = 250\mu$s are the input/output shift and the cycle task time respectively. Obviously, Eq. 4 is valid as long as the servomotor is run at steady state. For a generic motion law, the commanded position profile $\theta_{ref}(t)$ is stored in a vector and can therefore be employed for the calculation of θ_{est}. The computed M_{comp} is then transmitted to the drive unit, together with the motion set-point, i.e. θ_{ref} or ω_{ref} (see Fig. 2).

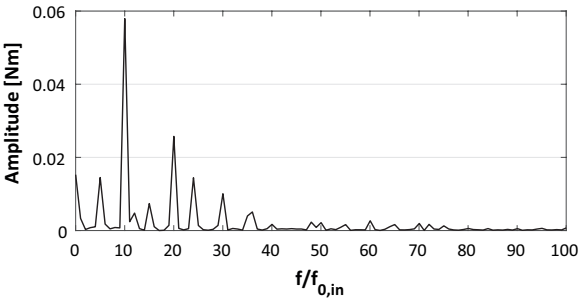

Figure 8: Spectrum of the registered torque ripples.

It is evident from Eq. 3 that a map of torque ripples versus rotor position must first be generated. The need to temporarily disengage the servomotor and operate it alone, together with the absence of frequency analysis and signal processing tools within the PLC environment (which always requires simplified code to work with real-time clock), makes it necessary to perform this step offline. In order to assure the best measurement condition, the torque ripples map is determined via the following steps:

1. disengage the servomotor from the mechanical transmission (i.e. no load applied);
2. move to the pre-defined home position;
3. activate the speed control mode;
4. set a low speed value (1rpm$\leq \omega_{ref} \leq$ 5rpm);
5. record the servomotor feedback (M_{mot} and θ_{mot}) for one complete revolution. To ensure constant speed in the range of interest, the experiment is performed between $-\delta\theta$ and $360°+\delta\theta$, where $\delta\theta$ is an extra angle (slightly greater than the distance traveled during the transients). A trigger signal is used to collect the data in 0° → 360° (forward motion) and 360° → 0° (backward motion).

During the post-processing, the acquired torque feedback is analyzed with the FFT tool in Matlab to evaluate its frequency content. According to the sampling theorem, with a sampling rate of 4000Hz, the FFT returns a maximum frequency of 2000Hz. For compensation purposes, this point deserves special attention. In fact, as the servomotor speed increases, the frequency of a position-dependent disturb increases and, at a specific point, it exceeds the upper bound (i.e. 2000Hz). As an example, the encoder-related peak at $f/f_{0,in} = 2048$ (where $f_{0,in} = \omega_{ref}/60$ represents the servomotor shaft frequency) appears in the spectrum only when the servomotor is operated at speed less than 58.6rpm. Hence, by considering this limit and a maximum rig operating speed of 2500rpm, the following analysis considers pulsations with $f/f_{0,in} \leq 2000/(2500/60) = 48$.

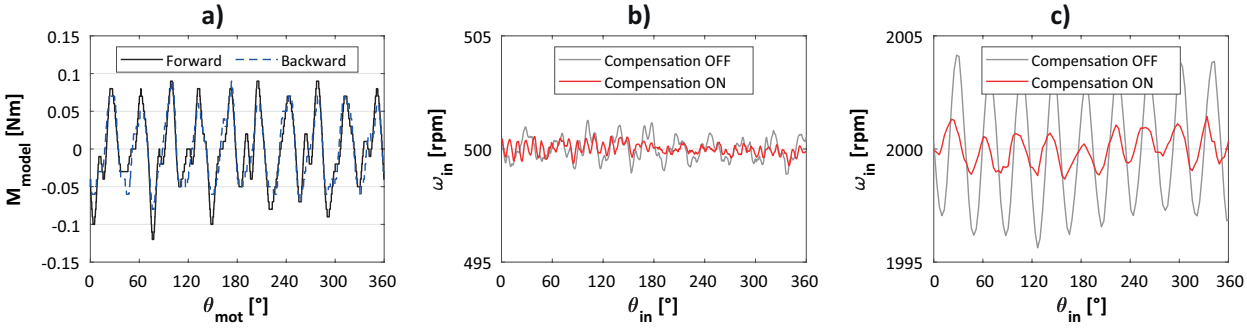

Figure 9: Torque ripples compensation: a) generated experimental model; b) test at 500rpm and c) test at 2000rpm.

The torque ripples spectrum is shown in Fig. 8, where the frequency axis is normalized with respect to $f_{0,in}$. The major components are multiples of the fundamental frequency, defined as $f_s = p\omega_{ref}/60 = pf_{0,in}$. The utilized servomotor has $p = 5$ pole pairs, thus $f_s/f_{0,in} = 5$. The noticeable peak at $f/f_{0,in} = 10$ forces the rig to vibrate when the servomotor works in the range $2000rpm \leq \omega_{mot} \leq 2250rpm$ (see Fig. 7). In this case, the excitation frequency equals 333.3Hz and 375Hz at $\omega_{mot} = 2000$rpm and 2250rpm respectively (i.e. close to the calculated f_n). The waveform also includes contributions at $f/f_{0,in} = \{12, 24, 36, 48\}$. For both positive and negative shaft rotations, the experimental model can be mathematically formulated as a Fourier series:

$$M_{model}(\theta) = \sum_{S} A_j \sin\left(j\theta + \Phi_j\right) \tag{5}$$

where S is the vector containing the selected contributions (from FFT analysis), whereas A_j and Φ_j are the amplitude and phase shift of the harmonic number j respectively. Figure 9a shows the resulting forward and backward compensation functions obtained from Eq. 5 with $S = \{5, 10, 12, 20, 24, 30, 36, 40, 48\}$. These are easily imported in the PLC project using text files. After restoring the connection between servomotor and reducer, a set of new tests has been performed by activating the proposed compensation scheme. To show the positive outcomes of the torque ripple compensation, comparisons are provided in Figs. 9b and c for both noncritical (500rpm, see Fig. 7a) and critical (2000rpm, Fig. 7c) working conditions. From the plotted speed feedback signals, a remarkable reduction (in the order of 60.1% and 69.3% for the case at 500rpm and 2000rpm respectively) of the oscillating amplitude can be observed, confirming the validity of the implemented approach. In light of these results, the torque ripple compensation has been kept on during the next experiments.

4. RV reducer experimental analysis

This section discusses the results of the experimental campaign, carried out after the rig tuning process, with the aim of characterizing the RV reducer performance. The main

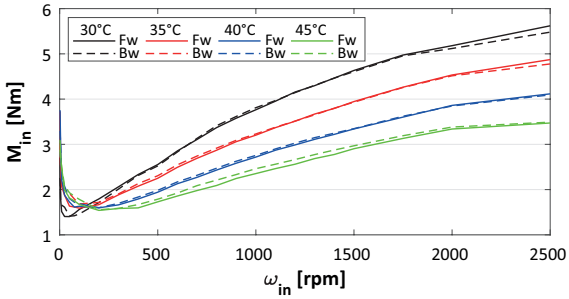

Figure 10: RV reducer friction load at different lubricant temperatures.

value of interest is the reducer TE function [22], defined as:

$$TE(\theta) = \theta_{out} - \frac{\theta_{in}}{\tau} \tag{6}$$

As discussed earlier, to exclude unwanted effects from the TE evaluation, e.g. the torsional compliance of the input transmission, θ_{in} and θ_{out} are directly read at the input and output side of the RV reducer. The TE is measured during forward and backward motions, obtaining two different curves, TE_f and TE_b. Their difference gives the so-called dynamic LM function:

$$LM(\theta) = TE_b - TE_f \tag{7}$$

where θ can be either θ_{in} or θ_{out}, though the latter option results more practical as it allows to express Eqs. 6 and 7 in the angular domain $[0, 360]°$. Such functions, in a more general form, should be written as $TE(\theta_{out}, \omega_{in}, T_l, M_{out})$ and $LM(\theta_{out}, \omega_{in}, T_l, M_{out})$, being $\omega_{in} = \partial\theta_{in}/\partial t$ the input speed and M_{out} the external applied load. This preliminary study mainly focuses on the combined effects of ω_{in} and T_l. The experiments have been performed with $M_{out} = 0$, namely by considering only the reducer internal friction torque.

4.1. Experimental procedures

An automated procedure has been coded at PLC level (*P_Experiment* script in Fig. 2) to control the sequence of operations and to execute multiple tests consecutively. The

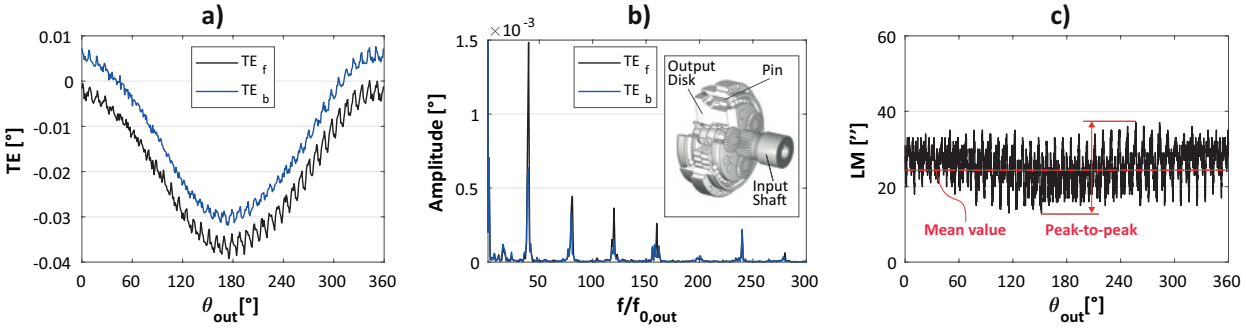

Figure 11: RV reducer transmission performance: a) forward and backward TE functions; b) TE spectrum and c) LM function.

experimental study is structured as a two-dimensional grid comprising all the possible combinations of the following array values:

- $\omega_{in} = \{5, 10, 25, 50, 75, 100, 200, 300, 400, 500, 750,$
  $1000, 1250, 1500, 1750, 2000, 2250, 2500\}$rpm
- $T_l = \{30, 35, 40, 45\}$°C

For each of the 72 experiments, the procedure involves the following basic steps:

1. A warm-up phase, where a continuous motion is performed ($\omega_{ref} = 1000$rpm if $T_l < 30$°C, 2000rpm otherwise) until the RV reducer oil temperature stabilizes at the specified value.
2. A homing procedure, consisting of three sub-steps. The reducer is first moved to reach the zero position of the output absolute encoder (θ_{out}). Then, slight corrections are made so as to position the input shaft in the middle of the angular backlash interval. The procedure concludes with the encoders zeroing.
3. Execution of the programmed test at constant speed for at least one complete revolution of the output side (i.e. until $\theta_{out} = 360°$). Similarly to Section 3.3, the motion is started/stopped considering an extra margin $\delta\theta$ to exclude the transients effects from the measurement interval. A trigger signal is used to validate the results when $\theta_{out} \in [0, 360]°$. After few instants, the backward motion is performed following the same protocol.
4. Export of the results array into a text file.

Before starting the first experiment, an additional preliminary step may become necessary to import/update the previously-defined compensating torque model M_{model}. Overall, the above mentioned procedure has proven to be solid and repeatable.

4.2. Results and discussion

The output vectors of the 72 experiments have been analyzed and plotted. At first, the reducer friction torque is evaluated. In the present case, considering minimal inertial contributions and null external loads ($M_{out} = 0$), the measured input torque corresponds to the reducer friction torque. The characteristic curves shown in Fig. 10 are simply generated by connecting the torquemeter feedback (mean values) acquired at different speeds. A close observation of the experimental plot leads to the following considerations:

- The reducer torque-speed characteristic shows a typical Stribeck effect (negative slope) at low speeds, as also documented in [22, 39, 45]. Then, once established the fluid lubrication stage, the friction torque increases linearly with the speed.
- The lubricant temperature strongly impacts the curves. In particular, an increasing temperature causes a reduction of the torque level and also the shift of the curve minimum (i.e. slope inversion point).
- The torques registered during forward and backward motions are in good agreement.

Overall, Fig. 10 provides clear indications regarding the need to consider T_l for the accurate modeling of RV reducers.

The acquired signals have been further processed based on Eqs. 6 and 7. In particular, exemplary graphs showing the TE and LM functions for $\theta_{out} \in [0, 360]°$ are reported in Fig. 11. The same figure also depicts the TE spectrum, where the frequency axis is normalized with respect to the output shaft frequency ($f_{0,out}$) to identify the main causes of errors in the reducer mechanism. In particular, in the range of one rotation of the output shaft, oscillations are seen at harmonics 1, 40 and multiples of 40. The harmonic 1 is most likely due to position deviation of the output disk, as also explained in [28], whereas the remaining ones are caused by the machining/assembly errors of the second reduction stage, being the total number of cycloidal gear teeth and pins respectively 39 and 40. Although TE_f and TE_b present peaks at the same frequencies, the curves do not perfectly match. The differences, mainly notable for $f/f_{0,out} \geq 40$ as also deduced from the resulting LM curve in Fig. 11c, indicate an asymmetric (i.e. direction dependent) tooth-pin contact interaction within the cycloidal stage. Similar spectral components can be observed with other Nabtesco RV reducers, namely RV-40E-121 and RV-80E-121, in [50] and [22, 32] respectively. Nevertheless, the different testing conditions (ω_{in} and T_l) as well the absence of open research data sets make it difficult to conduct detailed comparisons.

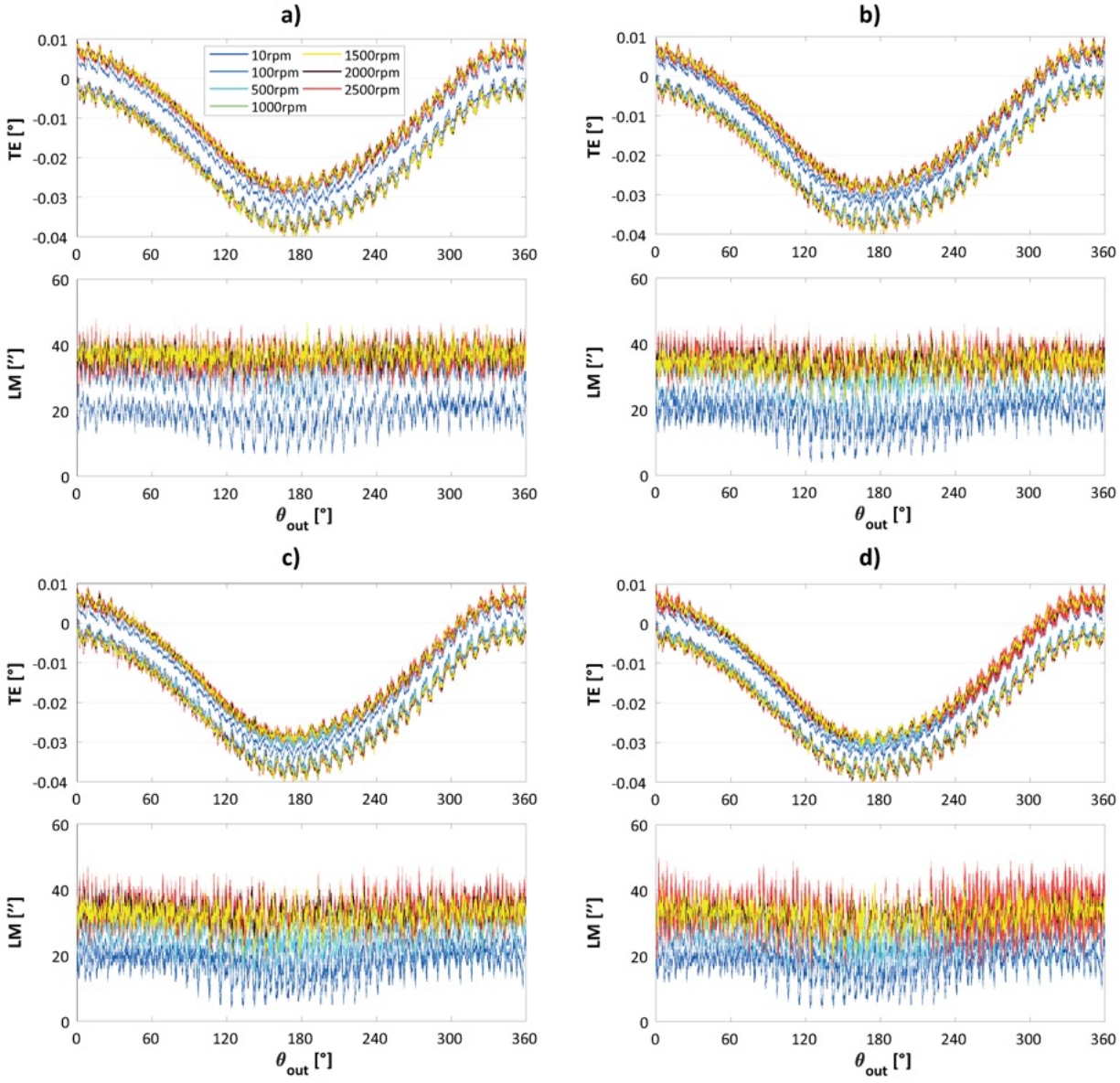

Figure 12: Experimental TE and LM functions at different lubricant temperatures: a) 30°C; b) 35°C; c) 40°C and d) 45°C.

The influence of ω_{in} and T_l on the reducer kinematic behavior can be observed in Fig. 12, where comparative plots of TE and LM are shown for all temperatures and seven speeds (10rpm, 100rpm, 500rpm, 1000rpm, 1500rpm, 2000rpm and 2500rpm). The measured TE presents notable differences in terms of curve depth (governed by $f/f_{0,out} = 1$) and meshing kinematic errors ($f/f_{0,out} \geq 40$). Generally, at higher speeds the LM trend results more flat. The LM mean value varies with the reducer friction torque, namely it increases when the input speed increases and/or when the oil temperature decreases, as clearly visible in Fig. 13. In the 72 experiments, the mean LM varies between $16.8''$ and $35.4''$. In all cases, the maximum measured LM is less than $45''$, similarly to [22]. At last, to prove the importance of implementing proper disturb compensation strategies (see Section 3.3), Fig. 14 reports the LM function measured at 2000rpm (i.e. same condition shown in Fig. 9c) with the compensation respectively disabled and enabled. It is worth noting that while the LM mean value remains unvaried, the peak-to-peak LM is reduced of 53%, namely from $40.6''$ to $19''$.

4.3. Experimental model

From the frequency response of the waveforms shown in Fig. 12, a simple mathematical formulation for TE_f and TE_b is defined as the sum of the main significant harmonics [30]:

$$TE_{\_,model}(\theta_{out}, \omega_{in}, T_l) = \sum_{P} A_{\_,k} \cos\left(k\theta_{out} + \Phi_{\_,k}\right) \tag{8}$$

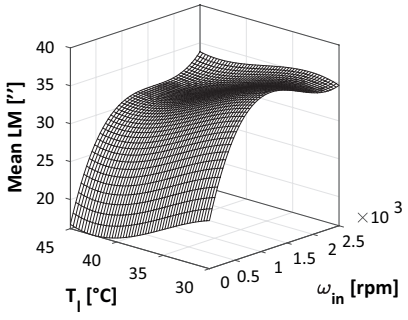

Figure 13: Experimental 3D map of the mean LM.

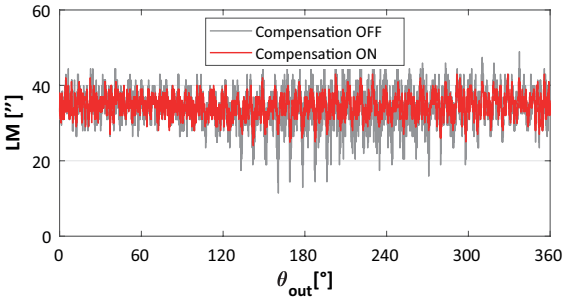

Figure 14: Effect of torque ripple compensation on the registered LM function ($\omega_{in} = 2000$rpm, $T_l = 35°$C).

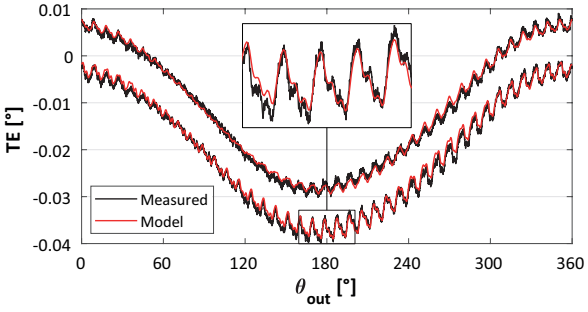

Figure 15: Comparative TE functions in experiment and model ($\omega_{in} = 500$rpm, $T_l = 30°$C).

being P the vector of the selected harmonic orders, $A_{\_,k}$ and $\Phi_{\_,k}$ the amplitude and phase shift of the harmonic k (subscript _ can be f or b, indicating forward and backward rotations respectively). More details about these quantities are given in the Appendix. By adopting $P = \{0, 1, 40, 80, 120, 160, 200\}$, Eq. 8 reproduces the reducer TE with acceptable accuracy (i.e. maximum error less than 5%), as it can be seen in the enlarged view of Fig. 15. If required, higher modeling quality can be achieved by including more contributions in P. The proposed model, which represents a valid tool for validating existing virtual prototypes or implementing kinematic compensation strategies in servomotor-side controlled SMs, is shared with the research community through an open dataset.

5. Conclusions

This paper reports about the performance evaluation of SMs employed in modern IRs. It has been conceived to reach a double scope: i) to present in details the developed measuring system and methods, and ii) to share and discuss the results achieved during the first experimental campaign. Hence, the first part of the work focuses on the description of the employed hardware and software tools, with particular emphasis placed on the data synchronization and on the effects introduced by the input transmission elasticity and reducer lubricant, the latter being particularly sensible from its operating temperature. It has been proposed a novel tuning strategy to stabilize the shaft speed before addressing detailed measurements of the reducer dynamic performance. By following a feedforward schematic, a practical method for the torque ripple suppression has been implemented in the proposed PLC-based system. Despite the need for further improvements, the presented approach allowed to decrease the input speed oscillations (in the order of 69.3% at 2000rpm), with a consequent 53% diminution of the reducer peak-to-peak LM. In the second part of the work, a grid-based parametric study with a total number of 72 experiments (as a combination of 4 temperatures and 18 input speeds) has been defined, which allowed to build comprehensive performance maps of the reducer. The outcomes highlighted a nonlinear dependency of the TE and LM characteristics from the reducer friction torque. An evident variability is also observed in the mean LM, which steps from $16.8''$ to $35.4''$ within the explored domain. The TE frequency content is consistent among the 72 candidates, although each peak differs in amplitude according to the adopted input speed and lubricant temperature. By selecting the most significant harmonic contributions, a mathematical model of the reducer TE is derived and shared for further developments.

Funding sources

This research was funded by the European Community's HORIZON 2020 programme under grant agreement No. 958303 (PENELOPE).

Appendix

A. Experimental model coefficients

For any combination of ω_{in} and T_l, Eq. 8 requires a novel set of coefficients ($A_{f,k}$, $A_{b,k}$, $\Phi_{f,k}$ and $\Phi_{b,k}$) to match the experimental TE curves. Therefore, the coefficients extrapolated via FFT from the 72 experiments are fitted using numerical approaches. Supposing to proceed with third order polynomial surfaces, one could derive empirical relations in

the following form:

$$A_{\_,k}(\omega_{in}, T_l) = \sum_{m=0}^{3} \sum_{n=0}^{3-m} p_{mn}\ \omega_{in}^{m} T_l^{n} \tag{9}$$

where p_{lm}, $l = \{0, 1, 2, 3\}$ $m = \{0, .., 3 - l\}$, are the fitting coefficients. The same formula is used for $\Phi_{\_,k}$. The total number of surfaces is $N = 4\ dim(P) - 2$, being the phase shift of the harmonic 0 (representing the TE mean value) null. Examples of fitting coefficients and the script for their generation are provided in the shared data set.

B. Supplementary data

The folder containing the experimental model can be freely downloaded via a Mendeley Data link from the online version of this paper.

References

[1] E. Oztemel, S. Gursev, Literature review of industry 4.0 and related technologies, Journal of Intelligent Manufacturing 31 (1) (2020) 127–182.

[2] A.-D. Pham, H.-J. Ahn, High precision reducers for industrial robots driving 4th industrial revolution: state of arts, analysis, design, performance evaluation and perspective, International journal of precision engineering and manufacturing-green technology 5 (4) (2018) 519–533.

[3] R. A. Boby, A. Klimchik, Combination of geometric and parametric approaches for kinematic identification of an industrial robot, Robotics and Computer-Integrated Manufacturing 71 (2021) 102142.

[4] M. Slamani, A. Nubiola, I. Bonev, Assessment of the positioning performance of an industrial robot, Industrial Robot: An International Journal (2012).

[5] M. Slamani, I. A. Bonev, Characterization and experimental evaluation of gear transmission errors in an industrial robot, Industrial Robot: An International Journal (2013).

[6] T. Cvitanic, S. N. Melkote, A new method for closed-loop stability prediction in industrial robots, Robotics and Computer-Integrated Manufacturing 73 (2022) 102218.

[7] L. McGarry, J. Butterfield, A. Murphy, Assessment of iso standardisation to identify an industrial robot's base frame, Robotics and Computer-Integrated Manufacturing 74 (2022) 102275.

[8] A. Nubiola, I. A. Bonev, Absolute calibration of an abb irb 1600 robot using a laser tracker, Robotics and Computer-Integrated Manufacturing 29 (1) (2013) 236–245.

[9] M. Slamani, I. A. Bonev, Characterization and experimental evaluation of gear transmission errors in an industrial robot, Industrial Robot: An International Journal (2013).

[10] T. Brogårdh, Robot control overview: An industrial perspective, Modeling, Identification and Control 30 (3) (2009) 167.

[11] M. Slamani, A. Nubiola, I. A. Bonev, Effect of servo systems on the contouring errors in industrial robots, Transactions of the Canadian Society for Mechanical Engineering 36 (1) (2012) 83–96.

[12] H. Schempf, Comparative design, modeling, and control analysis of robotic transmissions, Ph.D. thesis, Massachusetts Institute of Technology (1990).

[13] M. Piccoli, M. Yim, Anticogging: Torque ripple suppression, modeling, and parameter selection, The international journal of robotics research 35 (1-3) (2016) 148–160.

[14] S. Zhen, X. Peng, X. Liu, H. Li, Y.-H. Chen, A new pd based robust control method for the robot joint module, Mechanical Systems and Signal Processing 161 (2021) 107958.

[15] K. C. Yeo, G. Heins, F. De Boer, B. Saunders, Adaptive feedforward control to compensate cogging torque and current measurement errors for pmsms, 2011 IEEE International Electric Machines & Drives Conference (IEMDC) (2011) 942–947.

[16] M. Ruderman, M. Iwasaki, Sensorless torsion control of elastic-joint robots with hysteresis and friction, IEEE Transactions on Industrial Electronics 63 (3) (2015) 1889–1899.

[17] P. L. García, S. Crispel, E. Saerens, T. Verstraten, D. Lefeber, Compact gearboxes for modern robotics: A review, Frontiers in Robotics and AI 7 (2020) 103.

[18] A.-D. Pham, H.-J. Ahn, Rigid precision reducers for machining industrial robots, International Journal of Precision Engineering and Manufacturing (2021) 1–18.

[19] M. Ruderman, T. Bertram, M. Iwasaki, Modeling, observation, and control of hysteresis torsion in elastic robot joints, Mechatronics 24 (5) (2014) 407–415.

[20] T. Tjahjowidodo, F. Al-Bender, H. Van Brussel, Theoretical modelling and experimental identification of nonlinear torsional behaviour in harmonic drives, Mechatronics 23 (5) (2013) 497–504.

[21] N. G. Dagalakis, D. R. Myers, Adjustment of robot joint gear backlash using the robot joint test excitation technique, The international journal of robotics research 4 (2) (1985) 65–79.

[22] H. Xu, Z. Shi, B. Yu, H. Wang, Dynamic measurement of the lost motion of precision reducers in robots and the determination of optimal measurement speed, Journal of Advanced Mechanical Design, Systems, and Manufacturing 13 (3) (2019) JAMDSM0044–JAMDSM0044.

[23] C.-H. Huang, S.-J. Tsai, A study on loaded tooth contact analysis of a cycloid planetary gear reducer considering friction and bearing roller stiffness, Journal of Advanced Mechanical Design, Systems, and Manufacturing 11 (6) (2017) JAMDSM0077–JAMDSM0077.

[24] Z.-Y. Ren, S.-M. Mao, W.-C. Guo, Z. Guo, Tooth modification and dynamic performance of the cycloidal drive, Mechanical Systems and Signal Processing 85 (2017) 857–866.

[25] T. Li, X. An, X. Deng, J. Li, Y. Li, A new tooth profile modification method of cycloidal gears in precision reducers for robots, Applied Sciences 10 (4) (2020) 1266.

[26] J. Han, W. Li, Z. Qiao, Analysis of mixed lubrication characteristics of cycloid pin-wheel transmission, International Journal of Precision Engineering and Manufacturing 22 (3) (2021) 453–472.

[27] J. G. Blanche, D. C. H. Yang, Cycloid Drives With Machining Tolerances, Journal of Mechanisms, Transmissions, and Automation in Design 111 (3) (1989) 337–344.

[28] K.-Y. Wu, Y.-P. Shih, J.-J. Lee, Kinematic error analysis of the rotor vector gear reducer with machining tolerances, Journal of the Brazilian Society of Mechanical Sciences and Engineering 42 (11) (2020) 1–16.

[29] P. Mesmer, M. Neubauer, A. Lechler, A. Verl, Robust design of independent joint control of industrial robots with secondary encoders, Robotics and Computer-Integrated Manufacturing 73 (2022) 102232.

[30] M. Yamamoto, M. Iwasaki, H. Hirai, Y. Okitsu, K. Sasaki, T. Yajima, Modeling and compensation for angular transmission error in harmonic drive gearings, IEEJ Transactions on electrical and electronic engineering 4 (2) (2009) 158–165.

[31] A. Burisch, A. Raatz, Investigation and strategies for precision of miniaturized robots with micro gears, Assembly Automation (2011).

[32] Y. Yang, G. Zhou, L. Chang, G. Chen, A modelling approach for kinematic equivalent mechanism and rotational transmission error of RV reducer, Mechanism and Machine Theory 163 (2021) 104384.

[33] Y.-H. Yang, C. Chen, S.-Y. Wang, Response sensitivity to design parameters of RV reducer, Chinese Journal of Mechanical Engineering 31 (1) (2018) 1–13.

[34] M. Wikło, R. Król, K. Olejarczyk, K. Kołodziejczyk, Output torque ripple for a cycloidal gear train, Proceedings of the Institution of Mechanical Engineers, Part C: Journal of Mechanical Engineering Science 233 (21-22) (2019) 7270–7281.

[35] A. D. Pham, H.-J. Ahn, et al., Lost motion analysis of one stage cycloid reducer considering tolerances, International Journal of Precision Engineering and Manufacturing 17 (8) (2016) 1009–1016.

[36] H.-J. Ahn, B. M. Choi, Y. H. Lee, A.-D. Pham, Impact analysis of tolerance and contact friction on a RV reducer using FE method, International Journal of Precision Engineering and Manufacturing

(2021) 1–8.

[37] W. Bo, W. Jiaxu, Z. Guangwu, Y. Rongsong, Z. Hongjun, H. Tao, Mixed lubrication analysis of modified cycloidal gear used in the RV reducer, Proceedings of the Institution of Mechanical Engineers, Part J: Journal of Engineering Tribology 230 (2) (2016) 121–134.

[38] Z. Qiu, J. Xue, Review of performance testing of high precision reducers for industrial robots, Measurement 183 (2021) 109794.

[39] H. Xu, Z. Shi, B. Yu, H. Wang, Optimal measurement speed and its determination method in the transmission precision evaluation of precision reducers, Applied Sciences 9 (10) (2019) 2146.

[40] L. Chen, H. Hu, Z. Zhang, X. Wang, Application of nonlinear output frequency response functions and deep learning to RV reducer fault diagnosis, IEEE Transactions on Instrumentation and Measurement 70 (2020) 1–14.

[41] J. Xue, Z. Qiu, L. Fang, Y. Lu, W. Hu, Angular measurement of high precision reducer for industrial robot, IEEE Transactions on Instrumentation and Measurement 70 (2021) 1–10.

[42] B. Chen, C. Peng, J. Huang, A new error model and compensation strategy of angle encoder in torsional characteristic measurement system, Sensors 19 (17) (2019) 3772.

[43] Y. Cao, G. Liu, H. Yu, H. Mao, K. He, R. Du, A novel comprehensive testing platform of RV reducer, 2018 IEEE International Conference on Information and Automation (2018) 269–274.

[44] Z. Yu, Y. Zhang, Diagnosis of the coupling misalignment of the vertical comprehensive performance test instrument of high precision reducer for industrial robot, Measurement 185 (2021) 109939.

[45] M. Gadaleta, G. Berselli, M. Pellicciari, F. Grassia, Extensive experimental investigation for the optimization of the energy consumption of a high payload industrial robot with open research dataset, Robotics and Computer-Integrated Manufacturing 68 (2021) 102046.

[46] M. Gadaleta, M. Pellicciari, G. Berselli, Optimization of the energy consumption of industrial robots for automatic code generation, Robotics and Computer-Integrated Manufacturing 57 (2019) 452–464.

[47] M. Belloni, P. Bilancia, R. Raffaeli, M. Peruzzini, M. Pellicciari, Design of a test rig for tuning and optimization of high dynamics servo-mechanisms employed in manufacturing automation, Procedia Manufacturing 55 (2021) 48–55.

[48] C. Studer, A. Keyhani, T. Sebastian, S. Murthy, Study of cogging torque in permanent magnet machines, IAS'97. Conference Record of the 1997 IEEE Industry Applications Conference Thirty-Second IAS Annual Meeting 1 (1997) 42–49.

[49] F. Bu, Z. Yang, Y. Gao, Z. Pan, T. Pu, M. Degano, C. Gerada, Speed ripple reduction of direct-drive PMSM servo system at low-speed operation using virtual cogging torque control method, IEEE Transactions on Industrial Electronics 68 (1) (2020) 160–174.

[50] F. Zhang, P. Li, P. Zhu, X. Yang, W. Jiang, Analysis on dynamic transmission accuracy for RV reducer, MATEC Web of Conferences 100 (2017) 01003.